ISSN 1990-7931, Russian Journal of Physical Chemistry B, 2022, Vol. 16, No. 8, pp. 1384–1396. © Pleiades Publishing, Ltd., 2022.
Russian Text © The Author(s), 2022, published in Sverkhkriticheskie Flyuidy. Teoriya i Praktika, 2022, Vol. 17, No. 2, pp. 75–91.

Ni and Ni–Co Catalysts Based on Mixed Ce–Zr Oxides Synthesized in Isopropanol Medium for Dry Reforming of Methane

Yu. N. Bespalko[a, *] (ORCID: 0000-0003-0995-1526), V. E. Fedorova[a], E. A. Smal[a] (ORCID: 0000-0001-5068-8964), M. V. Arapova[a] (ORCID: 0000-0003-3103-904X), K. R. Valeev[a] (ORCID: 0000-0001-5981-5018), T. A. Krieger[a] (ORCID: 0000-0003-1464-2429), A. V. Ishchenko[a] (ORCID: 0000-0001-7183-3905), V. A. Sadykov[a] (ORCID: 0000-0003-2404-0325), and M. N. Simonov[a] (ORCID: 0000-0002-5161-5684)

[a] *Federal Research Center "Boreskov Institute of Catalysis," Siberian Branch, Russian Academy of Sciences, Novosibirsk, 630090 Russia*

**e-mail: bespalko@catalysis.ru*

Received May 5, 2022; revised May 20, 2022; accepted May 20, 2022

Abstract—Single-phase Ce–Zr oxides with a fluorite structure were synthesized by the solvothermal method in an isopropanol medium. Synthesis was performed at the supercritical parameters of isopropanol. The effect of the synthesis parameters on the characteristics of the obtained materials (specific surface area, morphology, particle size, phase composition) was established. Ni (5 wt %) and Ni + Co (5 wt %) were deposited at a ratio of 1 : 1 by incipient wetness impregnation. The structure and properties of samples were characterized by physicochemical methods, such as X-ray diffraction, Raman spectroscopy, high-resolution transmission electron microscopy, and temperature-programmed reduction by hydrogen. The dependences of the conversion of reagents (CH_4 and CO_2), the yield of hydrogen, and the Ce/Zr ratio in the Dry reforming of methane (DRM) reaction on the composition of catalysts were studied. The effect of the composition of a deposited metallic component and the Ce/Zr ratio in the support on the catalytic properties and catalysts stability in the DRM reaction was shown.

Keywords: cerium–zirconium oxides, solvothermal synthesis, isopropanol, dry methane reforming

DOI: 10.1134/S1990793122080048

INTRODUCTION

The increase in the anthropogenic production of greenhouse gases and their emissions leads to the retention of heat in the Earth's atmosphere and, as a consequence, to global warming. Dry reforming of methane (DRM) is an attractive method for the utilization of two greenhouse gases (CH_4 and CO_2) and their conversion into syngas with its further utilization as a feedstock for chemical industry or as a fuel [1–3]:

$$CH_4 + CO_2 \rightarrow 2CO + 2H_2, \quad \Delta H^0_{298} = 247.3 \text{ kJ/mol}.$$

It is known that DRM catalysts represent metal oxide systems, whose active metal may be selected from a broad spectrum of transition elements ranging from representatives of the platinum group (Pt, Pd, Rh, and Ru [4, 5]) to the more economically attractive Ni, Co, and Fe [6, 7]. At the present time, nickel-based catalysts are considered to be the most promising and cost-effective ones, and the studies on the search for an efficient DRM catalyst are focused on solving the problem of deactivation of these catalysts due to the sintering of their active metal and the formation of carbon. Based on the analysis of numerous studies, it is possible to distinguish two of the most efficient approaches for improving the stability of nickel-containing catalysts, such as the ones given here:

(1) The design of catalysts with strong metal—support interaction promoting coke gasification and the stabilization of the deposited metal particles in a highly disperse state; and

(2) The modification of the structure and properties of the metallic particle itself, e.g., by doping a catalyst with the second metal [8, 9].

In the first case, oxides containing highly reactive oxygen are selected as a support. The catalysts based on these oxides implement the bifunctional mechanism, in which a methane molecule is activated on a metal particle, and a CO_2 molecule is activated on support sites with the fast transfer of surface oxygen forms to the metal–support interface and the gasification of coke precursors [9, 10]. Oxides with a fluorite structure based on cerium–zirconium oxide solid solutions are widely studied as such supports [3, 6, 11, 12]. Detailed studies on the textural and transport properties of these supports on the catalytic activity of catalysts based on them in the DRM reaction have shown that their application provides the stable oper-

ation of a catalyst due to the decrease in the amount of formed carbon [13, 14]. Moreover, strong metal—support interaction which is for complex oxides of the type described above promotes the stabilization of an active metal in a disperse state to prevent sintering and, thereby, increase catalyst activity and decrease coking [15, 16]. The dispersity of nickel particles should promote a decrease in the amount of carbon deposits, as the formation of carbon by the methane decomposition reaction is structurally sensitive reaction and occurs on the ensembles of nickel atoms with a larger size than reforming of methane [17].

The second case concerns the creation of bimetallic catalysts, whose stability is increased due to the change in the size and morphology of metal particles, their propensity for segregation, and the electron state (oxidation level) of active metals and their reducibility [5, 18, 19]. The transition elements, among which cobalt appears to be the promising one, are also used as the second metal [20]. Due to their similar configurations, Co and Ni can easily form bimetallic alloy nanoparticles, which have better characteristics in the DRM reaction compared to monometallic catalysts, in particular, at low and medium temperatures [21]. The formation of a Ni–Co alloy leads to the splitting of nickel ensembles, whose size has an effect on the growth rate of carbon particles [17] and may be used to significantly decrease the amount of carbon deposits. In addition, it has been shown in a number of studies [22, 23] that cobalt more readily transits into a partially oxidized state due to its higher affinity to oxygen in the reaction conditions on interacting with the oxidizer CO_2 to form Co^{2+} sites in the immediate proximity to the CH_x particles adsorbed on Ni^0 particles; this also suppresses the route of their conversion into carbon deposits through gasification. The combination of experimental DRM reaction studies and calculations within the framework of density functional theory (DFT) [24] also demonstrate that bimetallic Ni–Co catalysts have an advantage over monometallic ones due to the distinction in the activation of C–H bonds on Ni, Co, and Ni–Co clusters, the optimal strength parameters for bonds with oxygen, and the efficiency of hydrogen cleavage on Ni–Co clusters.

It is well known that the method used for the synthesis of complex oxides has a significant effect on the properties of the synthesized materials (phase composition, particle size, and textural characteristics). However, despite numerous studies, the question on the specific features of the structure formation of mixed cerium–zirconium oxides in the process of preparation and its effect on the properties of DRM catalysts with these oxides as supports is still relevant. The most widely used methods for the synthesis of complex Ce–Zr oxides are solid-phase synthesis [25], the citrate method (Pechini method) [11, 26, 27], coprecipitation [6, 28], mechanoactivation [29], solgen technology [12, 30–32], and hydrothermal synthesis [33]. In contrast to the methods listed, synthesis with the use of supercritical (SC) fluids in a flow reactor is characterized by lower energy expenditures and simple implementation [34]. In recent years, the interest in this type of synthesis has significantly increased, and in particular, it has been shown that the nature of a solvent also has an appreciable effect on the composition and size of the synthesized cerium oxide particles, in addition to the synthesis conditions [35].

The mechanism of oxide formation in the process of hydrothermal synthesis incorporates two stages, such as the hydration of precursors containing metal ions and the further dehydration at a high temperature with the precipitation of oxides [36, 37]. Alcohols in a supercritical state are also of interest as solvents, as they have lower critical temperatures and pressures compared to water, and the conditions of attaining a supercritical state are individual for each alcohol. The use of SC alcohols is promotive for a high rate of nucleation with the further negligible growth of the formed nuclei to provide the formation of highly disperse oxides [38]. Hence, the nucleation rate can be controlled by varying the temperature and pressure to perform the synthesis of samples with the desirable characteristics.

The application of different alcohols as the solvent ensured the synthesis of highly disperse Ce–Zr oxide particles [39, 40]. The use of isopropanol with reductive properties also provides the synthesis of systems containing highly disperse metallic components [41].

Supports based on mixed cerium–zirconium oxides with different Ce : Zr ratios and varied doping cations (Ti, Nb) were synthesized in a flow reactor in our previous studies [42–46]. In contrast to the Pechini method, which gives impurity ZrO_2 phases in the samples, single-phase Ce–Zr–(Ti/Nb) mixed oxides have been obtained by their synthesis in SC isopropanol. It has been shown that the addition of a chelating agent, namely, acetyl acetone leads to the stabilization of colloid particles in solutions and, as a result, single-phase complex Ce–Zr oxides with a uniform distribution of components are formed. The Ni-containing catalysts based on the synthesized supports demonstrated a rather high activity in the DRM reaction.

This paper is devoted to the synthesis and study of bimetallic nickel–cobalt catalysts on an active support based on Ce–Zr mixed oxides with different Ce : Zr atomic ratios (3 : 1 and 1 : 1). The study is focused on the effect of the synthesis conditions, the textural and structural characteristics of complex oxides synthesized in an isopropanol medium at supercritical parameters for this solvent and cobalt as the second metal on the activity and stability of catalysts in the DRM reaction.

EXPERIMENTAL

Synthesis of Supports and Catalysts

Complex Ce–Zr oxides were synthesized by the solvothermal method; isopropanol was used in the process of synthesis as a major medium component. Synthesis was conducted at 285–400°C and a reaction system pressure of 12.0 MPa above the critical parameters of isopropanol.

The process was performed in a flow stainless steel reactor representing a steel capillary with an inner diameter of 4 mm. The contact time was varied from 1 to 1.5 s. In the process of synthesis, the reaction mixture flow rate was kept constant. The rate of the solvent flow, into which a solution of reagents was fed, is specified in the comment to Fig. 1. The volumetric ratios of the flows were constant in all the experiments. For example, at a solvent flow rate of $v_{solv} = 9$ mL/min, the flow rate of the salt solution v_{salt} was 5 mL/min, being equal to $v_{salt} =$ 3 mL/min at $v_{solv} = 5.4$ mL/min.

After the synthesis, the resulting suspension was sent to a cooled separator installed after the reactor and concentrated. The time of synthesis was determined based on the available separator volume as 50 min (85 min at a longer time of contact). After the synthesis, the pressure was decreased to the pressure at the room level by using the shutoff valves located after the separator. The obtained precipitate representing a mixture of metal oxides was taken out of the separator, separated from the mother solution by decantation, and dried at 200°C with further calcination at 700°C for 2 h in the air.

The used precursors of supports were cerium nitrate $Ce(NO_3)_3 \cdot 6H_2O$ (Reakhim, pure grade) and a zirconium isobutoxide ($Zr(OBu)_4$) solution in *n*-butanole (80 wt %, sigma-Aldrich). Cerium nitrate was dissolved in isopropanol (Vekton, pure grade), and zirconium isobutoxide was dissolved in *n*-butanol in a mixture with acetyl acetonate as a complexone; the molar concentrations of Ce and Zr compounds were 0.25 and 0.8–1 mol/L, respectively.

The catalysts were prepared by the incipient wetness impregnation of supports with nickel nitrate (Vekton, pure for analysis grade) and cobalt nitrate (Reakhim, pure for analysis grade). After impregnation, the samples were dried and calcined in air at 700°C for 2 h. The content of the metallic component (Ni or Ni–Co at a mass ratio of 1 : 1) in the catalyst was 5 wt %.

PHYSICOCHEMICAL STUDIES

The X-ray diffraction studies of the synthesized supports and catalysts were performed on a Bruker D8 Advance diffractometer with CuK_α radiation and a LynxEye position-sensitive detector within a scanning range of $2\theta = 10°–85°$ at a step of 0.05°. The Raman spectra of the samples were recorded on a Bruker RFS 100/S Raman Fourier spectrometer (Germany) with a radiation power of 100 mW, a resolution of 4 cm^{-1}, and collection of 300 scans.

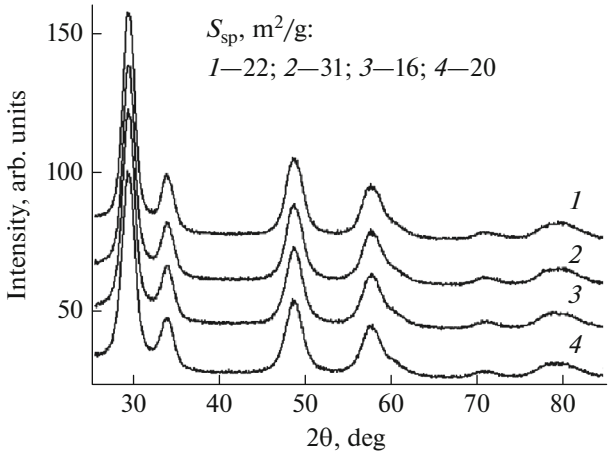

Fig. 1. X-ray diffraction patterns of $Ce_{0.5}Zr_{0.5}O_2$ oxide prepared under different conditions and corresponding values of specific surface area S_{sp} after calcination at 700°C: (*1*) 12.0 MPa, 285°C, $v_{solv} = 9$ mL/min, $v_{salt} = 5$ mL/min; (*2*) 12.0 MPa, 400°C, $v_{solv} = 9$ mL/min, $v_{salt} = 5$ mL/min; (*3*) 7.0 MPa, 285°C, $v_{solv} = 9$ mL/min, $v_{salt} = 5$ mL/min; (*4*) 12.0 MPa, 285°C, $v_{solv} = 5.4$ mL/min, $v_{salt} = 3$ mL/min.

The specific surface area was determined by the Brunauer–Emmett–Teller (BET) method from low-temperature nitrogen adsorption/desorption experiments performed on a Quadrasorb evo setup (Quantachrome Instruments, Unites States).

The reducibility of the supports and catalysts was studied by temperature-programmed reduction by hydrogen (H_2-TPR) with a linear temperature change (10 K/min) within a range of 60 to 900°C in an argon–10% hydrogen mixture; hydrogen consumption was determined by the heat conductivity detector of a Tsvet 500 chromatograph (Russia). Water was removed from the product by freezing at –80°C.

Images were taken by high-angle annular dark-field scanning electron microscopy (HAADF-STEM) and high-resolution transmission electron microscopy (HRTEM of TEM) on a JEM-2200FS transmission electron microscope (JEOL, Japan) (accelerating voltage, 200 kV; lattice resolution, 1 *A*) equipped with a Cs corrector and an energy dispersive (EDX) spectrometer (JEOL, Japan) with a Si- (Li-)detector for local elemental composition analysis (energy resolution, 130 eV). The minimum spot diameter for step-by-step line elemental EDX mapping analysis was ~1 nm with a step of nearly 1.5 nm.

The structure of Ni–Co catalysts before and after the DRM reaction was studied by transmission electron microscopy on a ThermisZ electron microscope (Thermo Fischer Scientific, United States) at an accelerating voltage of 200 kV. The microscope was equipped with a sample corrector for the correction of

spherical aberrations with the maximum lattice resolution of 0.06 nm. The images were recorded with a Ceta 16 CCD-detector (Thermo Fischer Scientific, United States).

Catalytic Tests

Catalytic tests were performed in a tubular quartz with an inner diameter of 4 mm which was installed in a furnace, where a thermocouple was placed into the annular space between the reactor and the furnace. To improve isothermicity in the catalyst bed, it was diluted with quartz at a mass ratio of 1 : 1 (0.5–0.25-mm catalyst–quartz sand fraction). Before the reaction, the catalysts were pretreated in a 10 vol % O_2–N_2 medium at 520°C for 30 min with further reduction at 520°C for 1 h in a 5 vol % H_2–He medium. In all the cases, the DRM reaction was performed at a reaction mixture composition of 15 vol % CH_4 + 15 vol % CO_2 in N_2, a contact time of 10 ms, and temperatures of 520, 575, 625, and 680°C with exposure of the catalyst at each temperature for 30 min. Prolonged tests were carried out at a contact time of 7.5. ms with exposure for 3 h at 630°C. The concentrations of the reagents and products were measured in the real-time regime on a Test-201 gas analyzer (Boner, Russia) equipped with IR optical, electrochemical, and polarographic sensors.

The conversions of reagents (X_i) were calculated by the formula

$$X_i(\%) = \frac{C_0 - C_i}{C_0} \times 100\%,$$

where C_0, C_i are the initial and final concentrations of the reagent, respectively (vol %);

$$Y(H_2)(\%) = 100C_{H_2}/2C^0_{CH_4},$$

where C_{H_2} is the hydrogen concentration in the reaction mixture, and $C^0_{CH_4}$ is the initial methane concentration.

RESULTS AND DISCUSSION

Physicochemical Properties of Supports and Catalysts

To optimize the method for the synthesis of catalyst supports in an isopropanol medium, four $Ce_{0.5}Zr_{0.5}O_2$ samples were synthesized by varying the synthesis parameters such as the reactor pressure, temperature, and solvent flow rate. According to the X-ray diffraction data (Fig. 1), the cubic CeO_2–ZrO_2 solid solution phase of the space group *Fm*3*m* with crystallites of size ~8 to 10 nm is formed after calcination at 700°C independently of the change in the synthesis parameters. An increase in the synthesis temperature results in a sample with a larger specific surface area. Hence, the optimal conditions of treatment in isopropanol, namely, 12.0 MPa, 400°C, and the flow rates v_{solv} = 9 mL/min and v_{salt} = 5 mL/min were selected for the further synthesis of catalysts.

According to the X-ray diffraction data (Fig. 2a), a fluorite-like cubic phase (PDF [81-0792) is formed for the $Ce_{0.5}Zr_{0.5}O_2$ and $Ce_{0.75}Zr_{0.25}O_2$ support samples. Moreover, the structure of complex oxides was additionally studied by Raman spectroscopy. As can be seen from Fig. 2b, the spectra of both supports contains a highly intense line at 470 cm^{-1}. It corresponds to the symmetric O–Ce–O vibration, i.e., the fundamental mode of F2g symmetry, which also confirms the existence of a phase with a cubic structure [47]. The additional band at 600 cm^{-1} is related to the formation of lattice defects, generally, oxygen vacancies [32, 48]. The intensity of bands I(D1 + D2) induced by defects in the region of 500 to 700 cm^{-1} is higher for the samples with a higher concentration of defects; thus, the ratio $\omega = I(D1 + D2)/I$F2g can be used as a parameter sensitive to defects. For the $Ce_{0.5}Zr_{0.5}O_2$ sample, this ratio ω is an order of magnitude higher (0.082) compared to the $Ce_{0.75}Zr_{0.25}O_2$ sample, which indicates the higher defectiveness of its structure. The Raman spectrum of $Ce_{0.5}Zr_{0.5}O_2$ also contains an additional low-intensity band typical for the tetragonal $Ce_{1-x}Zr_xO_2$ phase at 310 cm^{-1} [49].

Both studied CeO_2–ZrO_2 solid solution powders have similar morphologies representing spherical agglomerates assembled from finer differently oriented particles. According to the TEM data (Fig. 3), fluorite particles sizes range from 10 to 20 nm for both supports.

The study of the phase composition of the supported nickel catalysts prepared by the impregnation of complex Ce–Zr oxide powders with a nickel nitrate solution shows that all the samples represent well crystallized NiO particles on a fluorite-like support. The deposition of an active component has no effect on the unit cell parameter of the support (Table 1), which indicates that the deposited metal ions are not introduced into the fluorite crystal lattice. In the presented X-ray diffraction patterns (Fig. 4), reflections (111) and (200) corresponding to the NiO phase (PDF [65-2901]) can be clearly seen. The average size of NiO crystallites for all the catalysts was estimated from the integral broadening of reflection (200) by the Selyakov–Scherrer equation as ~20 nm. In bimetallic Ni–Co catalysts, the Co_3O_4 phase (PDF [043-1003]) was additionally detected; the size of crystalline cobalt oxide domains (the size of coherent scattering regions (CSR)) in the Ni–Co/$Ce_{0.75}Zr_{0.25}O_2$ and Ni–Co/$Ce_{0.5}Zr_{0.5}O_2$ samples was 55 and 50 nm, respectively.

The bimetallic catalysts reduced in hydrogen by the technique similar to the pretreatment of catalysts before the reaction were also studied by X-ray diffraction (Fig. 4). In the reduced catalysts, the formation of a nickel–cobalt alloy (PDF [004-8490]) is observed as

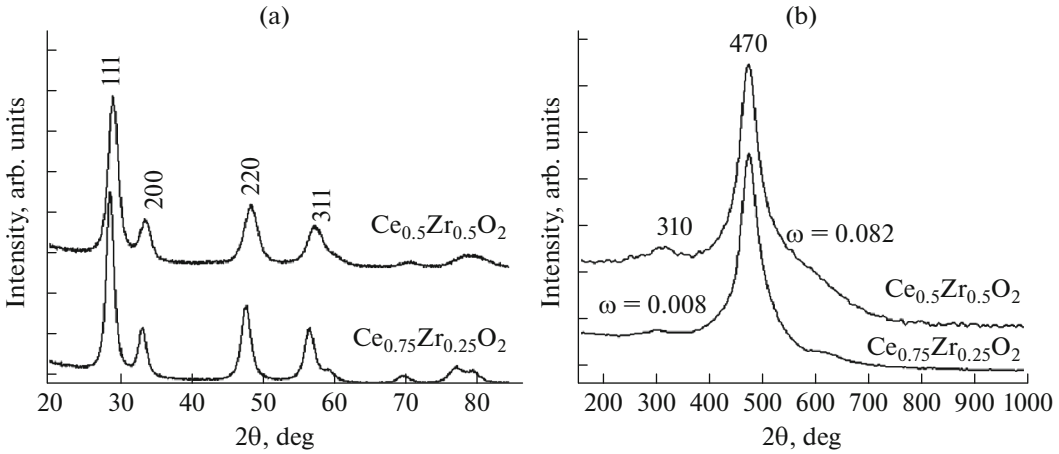

Fig. 2. (a) X-ray diffraction patterns and (b) Raman spectra of oxides $Ce_{0.75}Zr_{0.25}O_2$ and $Ce_{0.5}Zr_{0.5}O_2$ after calcination at 700°C.

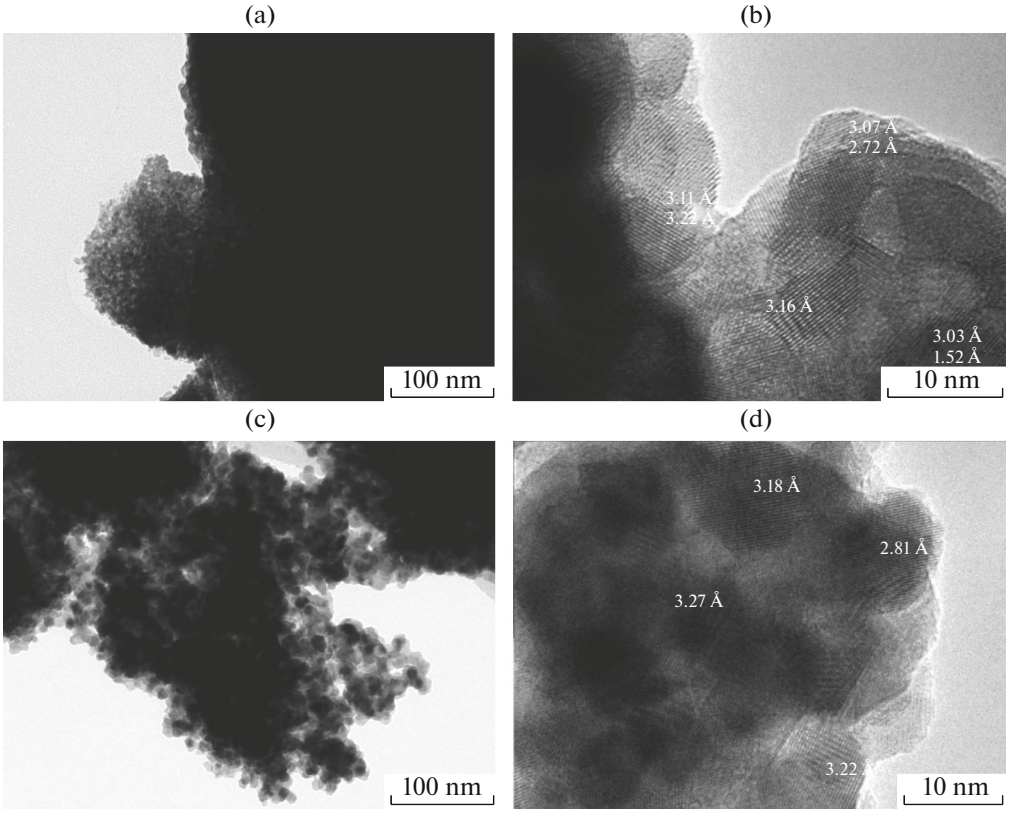

Fig. 3. TEM images of complex oxides (a), (b) $Ce_{0.5}Zr_{0.5}O_2$ and (c), (d) $Ce_{0.75}Zr_{0.25}O_2$.

indicated by the reflections at 44° and 51.7°. According to the X-ray diffraction data, the CSR size of nickel–cobalt alloys is 20 and 65 nm for Ni–Co/$Ce_{0.75}Zr_{0.25}O_2$ and Ni–Co/$Ce_{0.5}Zr_{0.5}O_2$, respectively. The unit cell parameter of the fluorite-like phase increases after the reduction of both catalysts (Table 1) probably due to the change in the Ce^{3+}/Ce^{4+} cation ratio. The increase in this parameter can be explained by the growth in the amount of Ce^{3+} ions, as their radius (1.14 Å) is larger than that for Ce^{4+} (0.97 Å) [50]. The CSR size for both compositions remains almost unchanged, which suggests the stability of the samples under sintering during reductive treatment.

After the deposition of metals, the measured specific surface area of all the catalysts decreases almost

Table 1. Phase composition and textural characteristics of samples

Composition	Unit cell parameter, Å	CSR size, nm				S_{BET}, m^2/g
		lattice parameter, Å	NiO	Co_3O_4	Ni–Co	
$Ce_{0.5}Zr_{0.5}O_2$	5.316	8.6	—	—	—	31
$Ni/Ce_{0.5}Zr_{0.5}O_2$	5.316(9)	8.6	19	—	—	14
$Ni–Co/Ce_{0.5}Zr_{0.5}O_2$	5.316(9)	8.7	22	50	—	12
	5.343(8)*	8.6		—	65	
$Ce_{0.75}Zr_{0.25}O_2$	5.368(1)	8.8	—	—	—	29
$Ni/Ce_{0.75}Zr_{0.25}O_2$	5.368(1)	9.4	20	—	—	21
$Ni–Co/Ce_{0.75}Zr_{0.25}O_2$	5.372(2)	9.3	23	55	—	20
	5.387(1)*	9.9	—	—	20	

* Samples reduced in H_2 at 600°C.

by factors of 1.5 to 2, apparently, due to the partial blocking of the pores [44]. The specific surface area after calcination at 700°C was ~20 m^2/g for the Ni- and $Ni–Co/Ce_{0.75}Zr_{0.25}O_2$ catalysts and only 12–14 m^2/g for the Ni- and $Ni–Co/Ce_{0.5}Zr_{0.5}O_2$ catalysts (Table 1).

According to the HAADF-STEM data (dark-field image in high-angle scattered electrons) (see Fig. 5, inset in color), the $Ni–Co/Ce_{0.75}Zr_{0.25}O_2$ sample contains agglomerates of mixed cerium–zirconium oxide particles of 50 to 200 nm with concentric inhomogeneities in the cerium concentration. The formation of spherical oxide (SiO_2, TiO_2, CeO_2, and ZrO_2) particles with radial inhomogeneity in their concentration under SC conditions in organic solvents was also shown by P. Wang et al. [40]. In our case, the use of a flow reactor and a mixture of polycationic precursors complicates the detailed study of nucleation kinetics, but it is quite possible to presume that there exists a similar regularity in the formation of particles due to the almost simultaneous heating of the mother solution of support precursors supplied to the synthesis medium. Despite the presence of composition inhomogeneities, the support is a single phase according to the X-ray diffraction data. It has been shown in the earlier paper [51] that the deposition of nickel onto supports with concentric inhomogeneities leads to its localization predominantly in the surface areas enriched with cerium, and this in turn promotes the growth of catalytic activity as can be seen from the example of the dry ethanol reforming reaction.

According to the TEM data for the $Ni–Co/Ce_{0.5}Zr_{0.5}O_2$ catalyst particles (Fig. 6, inset in color), there are no concentric inhomogeneities of cerium content. The distribution of cerium and zirco-

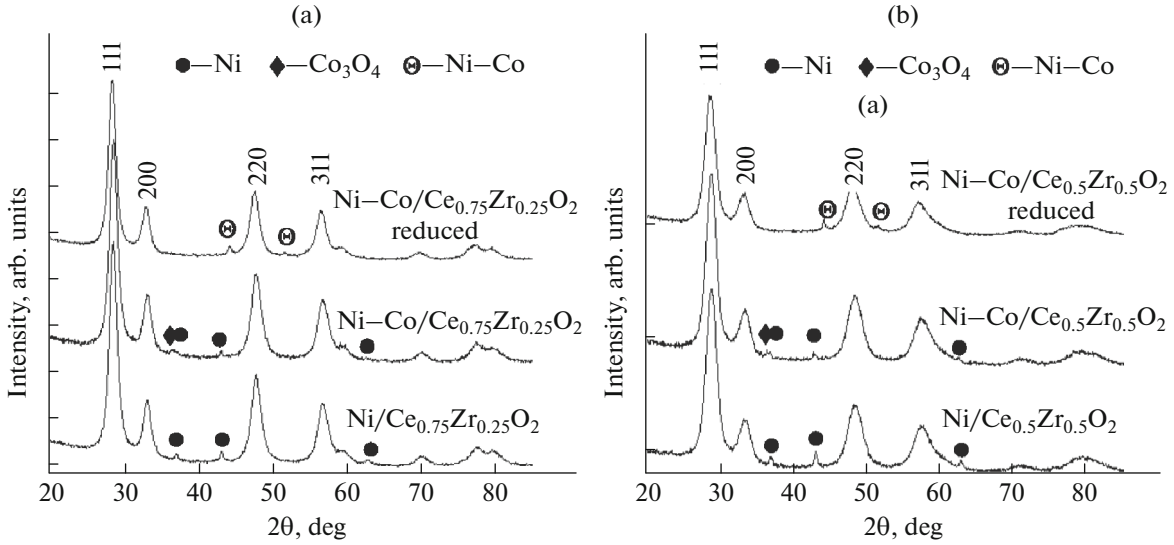

Fig. 4. X-ray diffraction patterns of supported catalysts based on (a) $Ce_{0.75}Zr_{0.25}O_2$ and (b) $Ce_{0.5}Zr_{0.5}O_2$ after calcination at 700°C and reduction in hydrogen at 600°C.

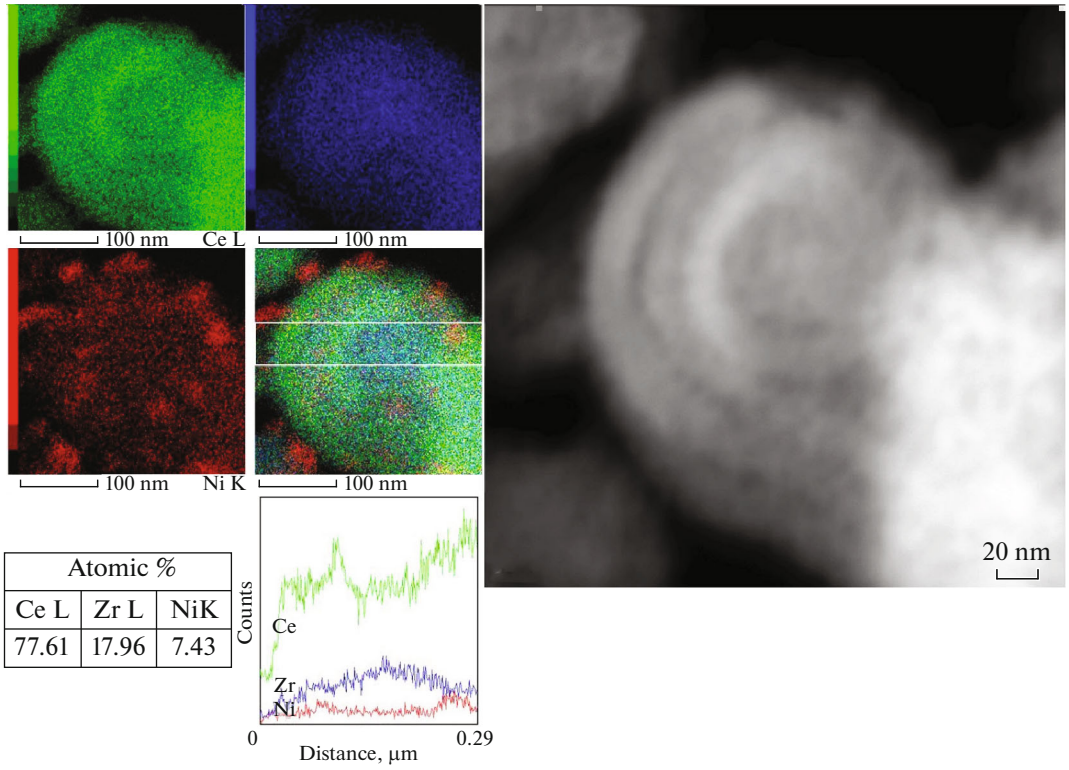

Fig. 5. HAADF-STEM images of the Ni/$Ce_{0.75}Zr_{0.25}O_2$ catalyst.

nium cations in the support is uniform, and nickel and cobalt oxide particles form agglomerates of 20 to 50 nm.

Reducibility (H_2-TPR)

The H_2-TPR curves for both supports and catalysts are shown in Fig. 7. The high-temperature low-intensity peak at 760–770°C corresponds to the partial reduction of Ce^{4+} to Ce^{3+} with the formation of oxygen vacancies [19]. The reduction curves of both supports have the peak corresponding to the removal of oxygen from the surface layers of Ce^{4+} oxide in the region of 536 to 564°C [15, 47]. The curves for the monometallic catalysts contain two hydrogen consumption peaks. The peak with the maximum temperature of 320°C ($Ce_{0.75}Zr_{0.25}O_2$) and 390°C ($Ce_{0.5}Zr_{0.5}O_2$) corresponds to the reduction of massive NiO particles to Ni^0 [12], and the second high-intensity peak with the maximum temperature of 459°C ($Ce_{0.75}Zr_{0.25}O_2$) and 500°C ($Ce_{0.5}Zr_{0.5}O_2$) can be assigned to the reduction of NiO crystallites, which strongly interact with the support [52].

It is well known that Co_3O_4 reduction represents a two-stage process $Co_3O_4 \rightarrow CoO \rightarrow Co^0$, and the reduction temperature decreases together with the size of particles [20, 40]. The overlapping peaks in the region of 297 to 407°C (Fig. 7) indicate the reduction of Ni^{2+} to Ni^0 and $Co^{2+/3+}$ to Co^0, respectively.

It is well known that an increase in the reduction temperature of the deposited metal oxides is provoked by the stronger metal–support interaction as observed in this case for the $Ce_{0.5}Zr_{0.5}O_2$ support [16].

The amount of hydrogen consumed in the process of reduction is given in Table 2. Based on these values, the degree of reduction was estimated for the deposited metal. For this purpose, the difference between the amount of hydrogen consumed by a catalyst and the support was calculated and compared with the amount of hydrogen, which would be required for the complete reduction of the deposited metals from their oxides $NiO \rightarrow Ni$ and $Co_3O_4 \rightarrow Co$. It has been shown that the deposited nickel is completely reduced to metal in the monometallic catalysts, but the degree of reduction for the Ni–$Co/Ce_{0.5}Zr_{0.5}O_2$ and Ni–$Co/Ce_{0.75}Zr_{0.25}O_2$ catalysts is 94 and 80%, respectively. The incomplete reduction of the metallic component in the case of bimetallic catalysts may be due to the fact that cobalt partially remains in the Co^{2+} state.

It is important to point out that the deposition of an active component may have an effect on the oxide support reduction depth; thus, the obtained values may be underestimated with respect to real degrees of reduction for the deposited metals, but it seems possible to compare these values with each other to reveal a common regularity.

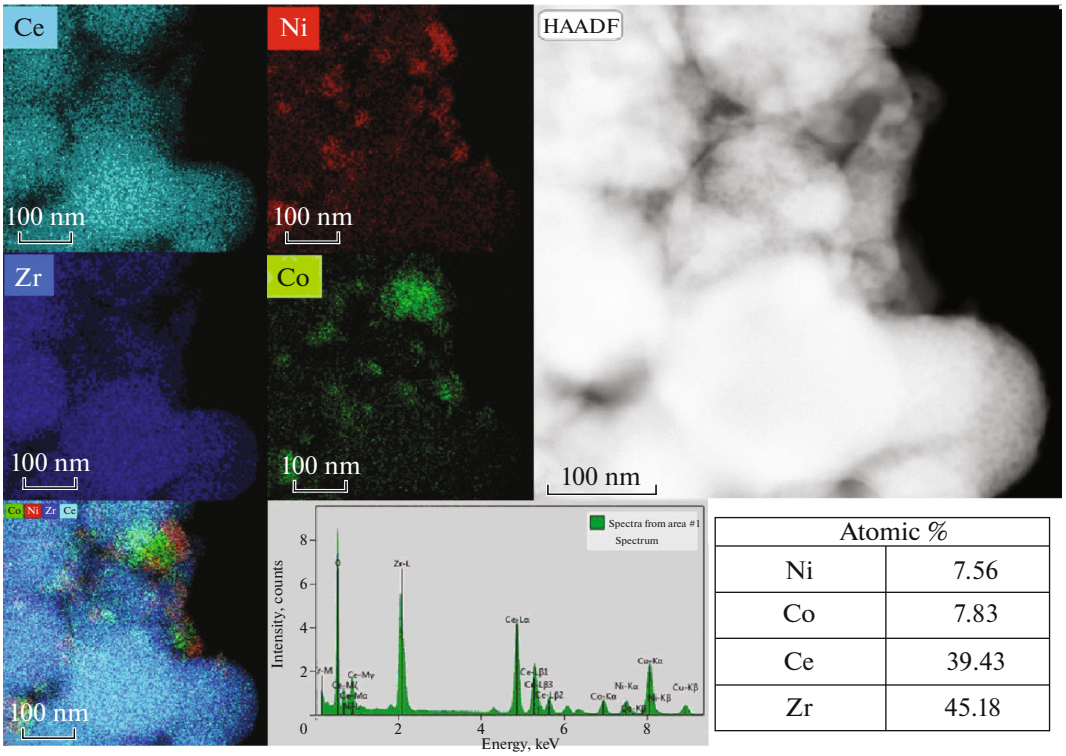

Fig. 6. HAADF-STEM images of the $Ni/Ce_{0.5}Zr_{0.5}O_2$ catalyst.

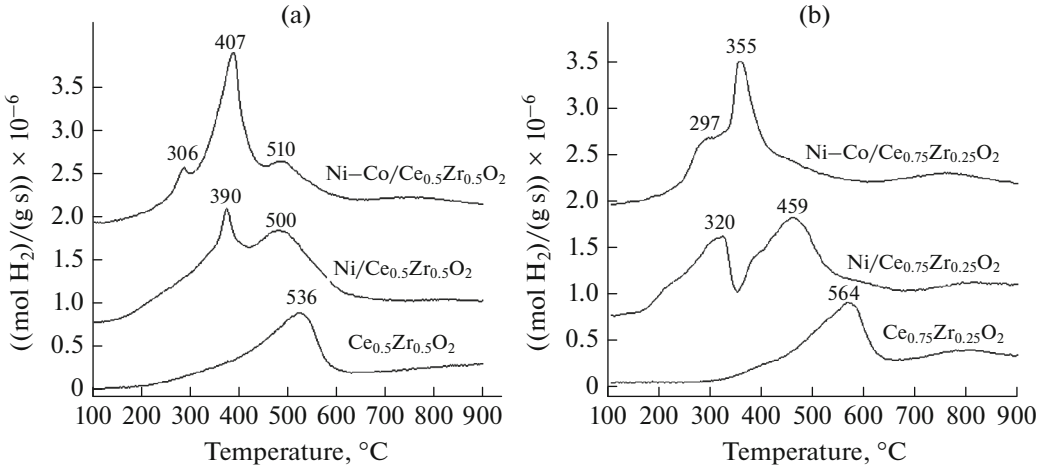

Fig. 7. H_2-TPR curves for supports and catalysts: (a) $Ce_{0.5}Zr_{0.5}O_2$, (b) $Ce_{0.75}Zr_{0.25}O_2$.

Catalytic Tests

The results of studying the activity of Ni- and Ni–Co catalysts based on the Ce–Zr supports in the DRM reaction are shown in Fig. 8 (see color embedding). It can be seen from Fig. 8 that the conversion of reagents and the yields of products increase with increasing temperature for all the samples. It can also be seen that the bimetallic catalysts are less active than the monometallic ones. The maximum methane conversion at 680°C is 45 and 41% for $Ni/Ce_{0.75}Zr_{0.25}O_2$ and $Ni/Ce_{0.5}Zr_{0.5}O_2$, respectively; however, the CO_2 conversion is higher than for methane and is almost the same for both catalysts. An essential difference between the CO_2 and CH_4 conversions throughout the entire range of studied temperatures takes place due to the effect of the side process in the system, i.e., the reverse water gas shift (steam CO conversion) reaction [32]

$$CO_2 + H_2 \rightarrow CO + H_2O.$$

Hydrogen reacts with CO_2 with the formation of CO and water which lead to a decrease in the H_2 : CO

Table 2. Hydrogen consumption during the temperature-programmed reduction of supports and catalysts

Composition	Consumed hydrogen amount, (mmol H_2)/g_{cat}	Δ*, (mmol H_2)/g_{cat}	Active component reduction degree, % from theoretical
$Ce_{0.5}Zr_{0.5}O_2$	1.34	–	–
$Ni/Ce_{0.5}Zr_{0.5}O_2$	2.22	0.88	103.5
$Ni–Co/Ce_{0.5}Zr_{0.5}O_2$	2.28	0.94	94
$Ce_{0.75}Zr_{0.25}O_2$	1.36	–	–
$Ni/Ce_{0.75}Zr_{0.25}O_2$	2.21	0.85	100
$Ni–Co/Ce_{0.75}Zr_{0.25}O_2$	2.16	0.8	80

* Difference between the hydrogen amounts consumed by a catalyst and a support.

ratio in the reaction product with respect to its theoretical value ($H_2/CO = 1$).

In addition, a regular change in catalytic properties is also observed depending on the Ce : Zr ratio in the oxide. The conversion and the yield of products are higher for the mono- and bimetallic catalysts on the $Ce_{0.75}Zr_{0.25}O_2$ support. In this case, both bimetallic $Ni–Co/Ce_{0.75}Zr_{0.25}O_2$ and $Ni–Co/Ce_{0.5}Zr_{0.5}O_2$ catalysts are less active than monometallic ones.

Since similar depths of reduction are observed for both supports according to the TPR data, the difference between the activities of catalysts based on the

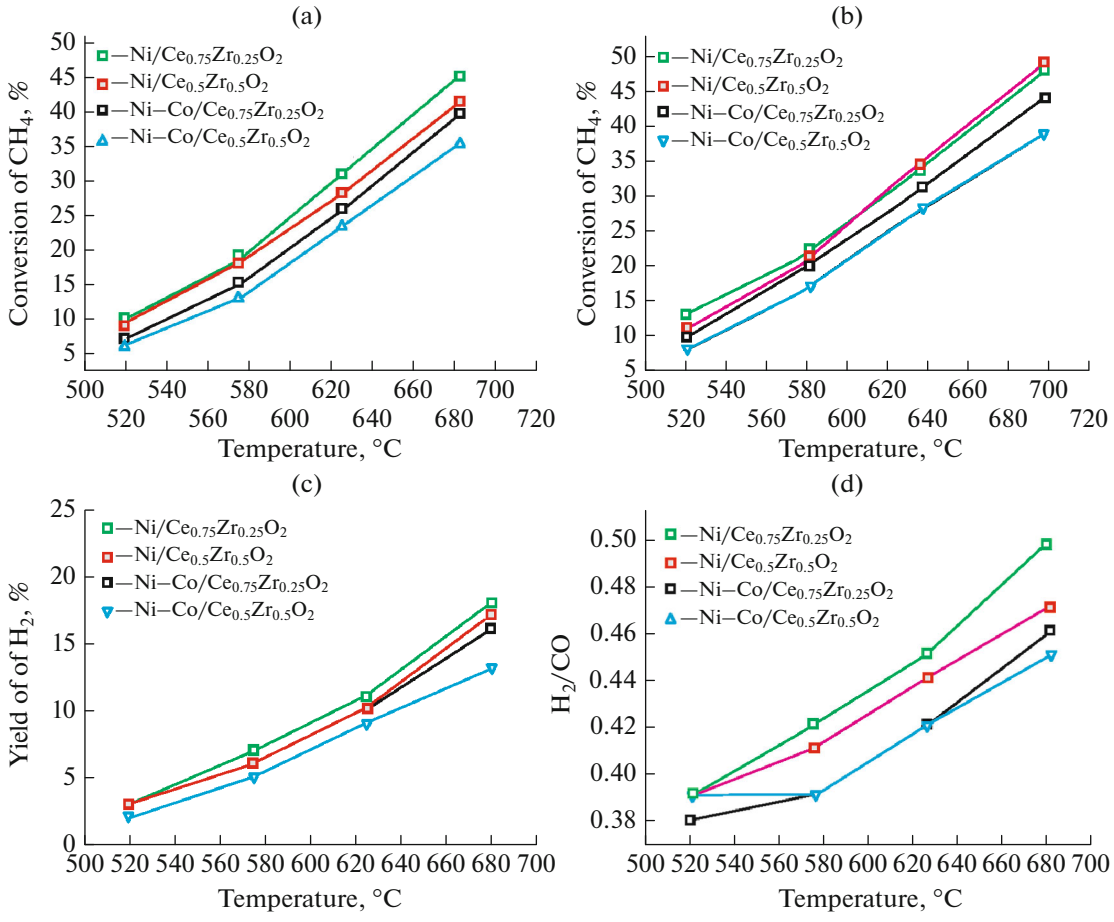

Fig. 8. (a) Methane and (b) CO_2 conversion, (c) hydrogen yield, and H_2/CO ratio versus temperature.

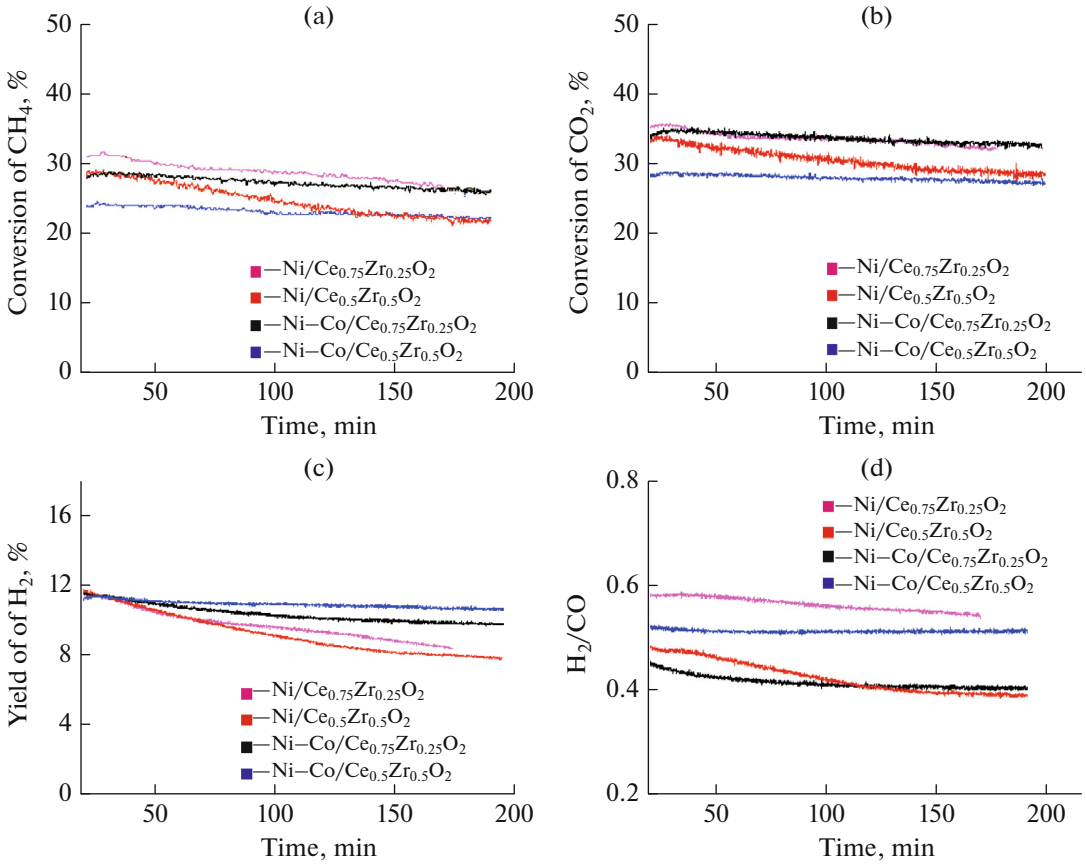

Fig. 9. (a) Methane and (b) CO_2 conversion, (c) hydrogen yield, and H_2/CO ratio versus DMR reaction time at 630°C.

supports with different Ce : Zr ratios may be due to the morphology of the deposited metal particles. In the case of bimetallic catalysts, the CSR size of alloy particles is 20 nm for Ni–Co/$Ce_{0.75}Zr_{0.25}O_2$ and 65 nm for Ni–Co/$Ce_{0.5}Zr_{0.5}O_2$. Hence, it is possible to assume that the higher activity for catalysts based on the $Ce_{0.75}Zr_{0.25}O_2$ support is due to a higher dispersity of the deposited metal particles.

Since the catalytic activity of nickel in the DRM reaction is higher than for cobalt [20, 23], the lower activity of catalysts with the deposited Ni + Co-active component takes place primarily due to the lower nickel concentration of their surface.

Short-term tests for stability were also performed for all the catalysts (Fig. 9, inset in color). The ratio between catalysts' activities remains unchanged for the first 30 min in the reaction mixture flow and coincides with the value obtained when studying the temperature dependence of the catalytic properties (Fig. 8). However, the activity decreases in the course of prolonged residence in the reaction medium, and this is accompanied by a decrease in the methane and CO_2 conversion. It is important to note that the decrease in activity is significant in the case of both monometallic catalysts. Bimetallic catalysts are more stable and, moreover, the hydrogen yield values remain constant and much higher than in the case of monometallic catalysts. This may be due just to the formation of alloys and, therefore, with the suppression of the formation of carbon deposits due to the dilution of nickel ensembles with cobalt. In addition, according to the H_2-TPR data, the depth of the reduction for bimetallic compositions is lower than for pure nickel, being in good agreement with the results of other authors and indicating the partial reduction of cobalt. It seems that the presence of cobalt promotes the activation of the oxidizer CO_2 in the immediate proximity to CH_x particles (coke precursors) and their further oxidation. There also exists the paper [22–24], where it is shown that cobalt more readily transits into the partially oxidized Co^{2+} state on interaction with CO_2 under the reaction conditions due to its slightly higher affinity to oxygen.

Among the bimetallic catalysts, a higher stability is also observed for the $Ce_{0.5}Zr_{0.5}O_2$ support, being in agreement with the stronger metal–support interaction shown by the comparison of the reduction profiles in the H_2-TPR experiments. Moreover, Raman

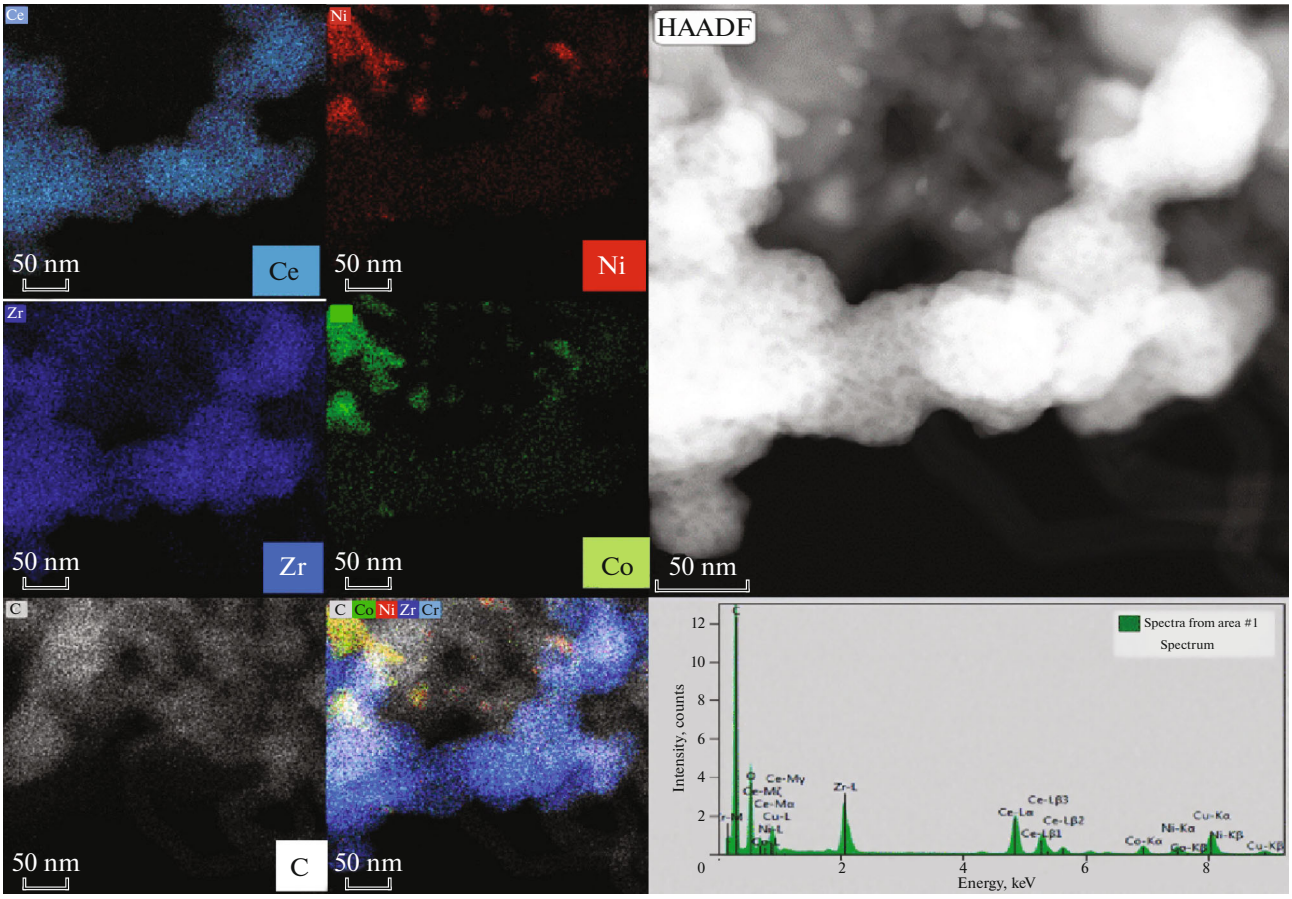

Fig. 10. HAADF-STEM images of the Ni–Co/$Ce_{0.5}Zr_{0.5}O_2$ catalyst after reaction.

spectroscopy has demonstrated that $Ce_{0.5}Zr_{0.5}O_2$ has high defectiveness and oxygen vacancies in the fluorite structure, which may also improve the resistance to coking. This was earlier demonstrated on the supports synthesized in an isopropanol medium [43, 44].

The HAADF-STEM images of the Ni–Co/$Ce_{0.5}Zr_{0.5}O_2$ catalyst after the DMR reaction are shown in Fig. 10 (see inset in color). Elemental analysis data confirm the formation of carbon. In this case, an Ni–Co alloy is observed on the support surface, being in good agreement with the X-ray diffraction analysis data.

CONCLUSIONS

The (Ce–Zr)O_2 supports with different molar Ce : Zr ratios (3 : 1 and 1 : 1) are synthesized by the solvothermal method at temperatures and pressure above the critical parameters of the medium's main component, isopropanol. It has been shown that synthesis process results in the formation of ultradisperse particles of oxides with the uniform distribution of cations as an advantage of synthesis in this medium. Using Raman spectroscopy, significant defectiveness in the fluorite structure has been shown. The high hydrogen consumption values in the process of the temperature-programmed reduction in both low- and high-temperature regions indicate a high content of reactive oxygen on the surface of oxide and in its volume.

The obtained oxides were used as supports for the synthesis of nickel and nickel–cobalt catalysts with an overall metal content of 5 wt %. The study of their catalytic properties in the dry reforming of methae reaction has shown that the Ni-containing monometallic catalysts exhibit much higher activity and selectivity due to the high nickel concentration on their surface. Bimetallic catalysts are much more stable than the mononickel catalysts due to the dilution of ensembles of nickel atoms with cobalt atoms, which partially retain their oxidized state. In this case, among the bimetallic catalysts, the maximum stability (the absolute absence of deactivation after 3 h of DMR reaction) is observed for the $Ce_{0.5}Zr_{0.5}O_2$ based catalyst, for which stronger metal–support interaction was observed according to the H_2-TPR data.

ACKNOWLEDGMENTS

The authors thank the Shared Facilities Center "High Technologies and Analytics of Nanosystems" of Novosibirsk State University for conducting the measurements on their scientific equipment.

FUNDING

This study was performed as part of project no. 18-73-10167 of the Russian Science Foundation.

REFERENCES

1. W.-J. Jang, J.-O. Shim, H.-M. Kim, S.-Y. Yoo, and H.-S. Roh, Catal. Today **324**, 15 (2019).
2. M. Aresta and A. Dibenedetto, Dalton Trans., 2975 (2007).
3. E. le Sache and T. R. Reina, Prog. Energy Combust. Sci. **89**, 10970 (2022).
4. D. Pakhare and J. Spivey, Chem. Soc. Rev. **43**, 7813 (2014).
5. I. V. Yentekakis and G. A. Panagiotopoulou, Appl. Catal. B: Environ. **296**, 120210 (2021).
6. A. Kambolis, H. Matralis, A. Trovarelli, and Ch. Papadopoulou, Appl. Catal. A: Gen. **377**, 16 (2010).
7. Y. Lyu, J. Jocz, R. Xu, E. Stavitski, and C. Sievers, ACS Catal. **10**, 11235 (2020).
8. M. A. Salaev, L. F. Liotta, and O. V. Vodyankina, Int. J. Hydrogen Energy **47**, 4489 (2022).
9. M. A. Vasiliades, P. Djinovi, L. F. Davlyatova, A. Pintar, and A. M. Efstathiou, Catal. Today **299**, 201 (2018).
10. Y. Khani, F. Bahadoran, Z. Shariatinia, M. Varmazyari, and N. Safari, Ceram. Int. **46**, 25122 (2020).
11. I. Luisetto, S. Tuti, C. Romano, M. Boaro, E. Di, J. Kopula, S. Senthil, and K. Selvakumar, J. CO_2 Util. **30**, 63 (2019).
12. J. A. Montoya, E. Romero-Pascual, C. Gimon, P. del Angel, and A. Monzin, Catal. Today **63**, 71 (2000).
13. L. Wu, X. Xie, H. Ren, and X. Gao, Mater. Today: Proc. **42**, 153 (2021).
14. S. Das, A. Jangam, S. Jayaprakash, S. Xi, K. Hidajat, K. Tomishige, and S. Kawi, Appl. Catal. B: Environ. **290**, 119998 (2021).
15. C. Pizzolitto, E. Pupulin, F. Menegazzo, E. Ghedini, A. di Michele, M. Mattarelli, G. Cruciani, and M. Signoretto, Int. J. Hydogen Energy **44**, 28065 (2019).
16. S. Bernal, J. J. Calvino, M. A. Cauqui, J. M. Gatica, C. Lopez Cartes, J. A. Perez Omil, and J. M. Pintado, Catal. Today **77**, 385 (2003).
17. C. M. Damaskinos, J. Zavasnik, P. Djinovic, and A. M. Efstathiou, Appl. Catal. B: Environ. **296**, 120321 (2021).
18. L. P. Teh, H. D. Setiabudi, S. N. Timmiati, M. A. A. Aziz, N. H. R. Annuar, and N. N. Ruslan, Chem. Eng. Sci. **242**, 116606 (2021).
19. J. Sasson Bitters, T. He, E. Nestler, S. D. Senanayake, J. G. Chen, and C. Zhang, J. Energy Chem. **68**, 124 (2022).
20. F. Sharifianjazi, A. Esmaeilkhanian, L. Bazli, S. Eskandarinezhad, S. Khaksar, P. Shafiee, M. Yusuf, B. Abdullah, P. Salahshour, and F. Sadeghi, Int. J. Hydrogen Energy (2021, in press).
21. Z. Wu, B. Yang, S. Miao, W. Liu, J. Xie, S. Lee, M. J. Pellin, D. Xiao, D. Su, and D. Ma, ACS Catal. **9**, 2693 (2019).
22. S. Sengupta, K. Ray, and G. Deo, Int. J. Hydrogen Energy **39**, 11462 (2014).
23. X. Li, J. Ai, W. Li, and D. Li, Front. Chem. Eng. China **4**, 476 (2010).
24. W. Tu, M. Ghoussoub, C. V. Singh, and Y. H. C. Chin, J. Am. Chem. Soc. **139**, 6928 (2017).
25. D. P. F. Souza, C. L. de Silva, and V. R. Mastelaro, J. Eur. Ceram. Soc. **23**, 273 (2003).
26. T. G. Kuznetsova and V. A. Sadykov, Kinet. Catal. **49**, 840 (2008).
27. A. le Gal, S. Abanades, and G. Flamant, Energy Fuels **25**, 4836 (2011).
28. A. N. Kharlanov, A. O. Turakulova, A. V. Levanov, and V. V. Lunin, Russ. J. Phys. Chem. A **92**, 678 (2018).
29. F. Zamar, A. Trovarelli, C. de Leitenburg, and G. Dolcetti, Studies Surf. Sci. Catal. B **101**, 1283 (1996).
30. E. A. Trusova, A. A. Khrushcheva, and K. V. Vokhmintcev, J. Eur. Ceram. Soc. **32**, 1977 (2012).
31. A. Horváth, G. Stefler, O. Geszti, A. Kienneman, A. Pietraszek, and L. Guczi, Catal. Today **169**, 102 (2011).
32. I. Luisetto, S. Tuti, and E. di Bartolomeo, Int. J. Hydrogen Energy **37**, 15992 (2012).
33. M. Hirano and E. Kato, J. Ceram. Soc. Jpn. **104**, 958 (1996).
34. A. A. Galkin and V. V. Lunin, Russ. Chem. Rev. **74**, 21 (2005).
35. C. Slostowski, S. Marre, O. Babot, T. Toupance, and C. Aymonier, Langmuir **28**, 16656 (2012).
36. Y. Hakuta, H. Hayashi, and K. Arai, Curr. Opin. Solid State Mater. Sci. **7**, 341 (2003).
37. A. Cabanas, J. A. Darr, E. Lester, and M. Poliakoff, Chem. Commun., 901 (2000).
38. J. A. Darr and M. Poliakoff, Chem. Rev. **99**, 495 (1999).
39. E. K. C. Pradeep, T. Habu, H. Tooriyama, M. Ohtani, and K. Kobiro, J. Supercrit. Fluids **97**, 217 (2015).
40. P. Wang, K. Ueno, H. Takigawa, and K. Kobiro, J. Supercrit. Fluids **78**, 124 (2013).
41. S. P. Gubin and E. Yu. Buslaeva, Russ. J. Phys. Chem. B **3**, 1172 (2009).
42. M. Y. Smirnova, S. N. Pavlova, T. A. Krieger, Y. N. Bespalko, V. I. Anikeev, Y. A. Chesalov, V. V. Kaichev,

M. V. Mesetseva, and V. A. Sadykov, Russ. J. Phys. Chem. B **11**, 1312 (2017).

43. Y. Bespalko, E. Smal, M. Simonov, K. Valeev, and V. Fedorova, Energies **13**, 3365 (2020).
44. M. Simonov, Y. Bespalko, E. Smal, K. Valeev, V. Fedorova, T. Krieger, and V. Sadykov, Nanomaterials **10**, 1 (2020).
45. A. Auxéméry, B. B. Frias, E. Smal, K. Dziadek, G. Philippot, P. Legutko, M. Simonov, S. Thomas, A. Adamski, V. Sadykov, K. Parkhomenko, A.-C. Rogerb, and C. Aymonier, J. Supercrit. Fluids **162**, 104855 (2020).
46. V. Fedorova, M. Simonov, K. Valeev, Y. Bespalko, E. Smal, N. Eremeev, E. Sadovskaya, T. Krieger, and A. Ishchenko, Energies **14**, 2973 (2021).
47. V. Sánchez Escribano, E. Fernández, M. Panizza, C. Resini, J. M. Gallardo Amores, and G. Busca, Solid State Sci. **5**, 1369 (2003).
48. A. Romero-Núñez and G. Diaz, RSC Adv. **5**, 54571 (2015).
49. M. Y. Smirnova, A. S. Bobin, S. N. Pavlova, A. V. Ishchenko, A. V. Selivanova, V. V. Kaichev, S. V. Cherepanova, T. A. Krieger, M. V. Arapova, A.-C. Rogerb, A. Adamski, and V. A. Sadykov, Open Chem. **15**, 412 (2017).
50. R. D. Shannon, Acta Crystallogr., Sect. A **32**, 751 (1976).
51. M. Arapova, E. Smal, Y. Bespalko, V. Fedorova, K. Valeev, S. Cherepanova, A. Ischenko, V. Sadykov, and M. Simonov, Int. J. Hydrogen Energy **46**, 39236 (2021).
52. H. Roh, K. Young, and W. Lai, Catal. Today **146**, 71 (2009).

Translated by E. Glushachenkova